International Journal of Microwave and Wireless Technologies

cambridge.org/mrf

Electrically small band-switchable antenna system for on-body applications

Niklas Takanen[1], Kimmo Rasilainen[1], Juha Katajisto[2], Aarno Pärssinen[1] and Ping Jack Soh[1]

[1]Centre for Wireless Communications, University of Oulu, Oulu, Finland and [2]Engineering Services, Bittium, Tampere, Finland

Research Paper

Cite this article: Takanen N, Rasilainen K, Katajisto J, Pärssinen A, Soh PJ (2026) Electrically small band-switchable antenna system for on-body applications. *International Journal of Microwave and Wireless Technologies* **18**(3), 483–497. https://doi.org/10.1017/S1759078726103225

Received: 31 October 2025
Revised: 10 April 2026
Accepted: 13 April 2026
First published online: 15 May 2026

Keywords:
aperture tuning; body phantom; electrically small antennas; measurements; specific absorption rate (SAR); wearable devices; 5G NR

Corresponding author: Niklas Takanen; Email: niklas.takanen@oulu.fi

Abstract

This work proposes a band-switchable electrically small antenna (ESA) system for a wearable health monitoring device. The system operates at multiple 5G-NR bands (875–934 MHz and 1.72–2.2 GHz) using a switchable configuration. The antenna consists of multi-resonant shorted strips that have been miniaturized to fit in meandered form into an area of $63.2\times25\,\text{mm}^2$ ($0.19\times0.08\lambda^2$) available in the intended health monitoring device. To enable operation at two distinct modes, the antenna feedline has been integrated with a switch, which is then matched using lumped matching components. Results indicate that the ESA system operates at 875–900 MHz in Configuration 1, and at 898–934 MHz and at 1.72–2.2 GHz in Configuration 2. The device has been fabricated and integrated into a compact 3D printed casing prior to experimental evaluations. In addition to studying the switchable reflection and radiation performance, the ESA is also evaluated in the presence of a human body phantom. Simulated specific absorption rate levels are less than 0.47 W/kg averaged over 1 g of tissue, which complies with international standards.

Introduction

Electrically small antennas (ESAs) with wide bandwidth at frequencies below 1 GHz are key technology enablers for the independent operation of portable and wearable devices. For instance, current 5G new radio frequency range 1 (5G NR FR1) standards require wireless devices operating within the frequency range of 699–960 MHz for low-band communications. Achieving good performance at these frequencies remains the main design challenge for compact communication devices such as mobile phones [1, 2], health monitoring, and Internet of Things devices. Due to this need, ESAs are gaining more significant importance with the advent of wearable devices and an increasing interest in wearable health technology.

The placement of the ESAs on the body of the user and their physical size limitations restrict efficient radiation performance. User effects need to be considered and characterized during the design phase, both in terms of how the body affects the antenna performance and how the antenna affects the user. Most importantly, wearable antennas require the designer to ensure consistent performance when operated near the human body, while operating within the specific absorption rate (SAR) limits set by safety standards [3]. These are optimized considering the dimension restrictions of the antenna within the device itself and how the device is located on the human body.

Research into antennas for wearable devices has mainly focused on compact, low-profile antennas that enable small and unobtrusive wearable devices. Cloud and edge computing shift the computing resource requirements further from the wearable device itself onto a remote server or edge node [4], which, together with the small wearable devices, will make it possible to support "device-less" wireless communications in the near future. This device is aimed to sense physiological parameters and wirelessly communicate them off-body. Nevertheless, the development of such a form of integration into wearable devices is taking place gradually, with devices being designed and packaged to be worn and operating closer to the human body. As a result, factors such as user comfort and safety must be considered, which subsequently leads to the need for ESAs and the need to study their SAR levels to ensure sufficient radiation safety margins and to maximize the energy transfer between the device and the base station [5, 6].

ESAs can be used to partially solve the limitations of wearable antennas by making use of their inherently small size. However, their use presents new challenges, such as low efficiency and reduced gain [7]. Moreover, further efficiency degradation is expected when operating close to the human body, relative to free space conditions. This degradation is expected to be as high as 3 dB compared to basic monopole- and planar inverted-F (PIFA) based antennas [8]. Such degradation is also obvious in state-of-the-art antennas and ESAs when operating a wearable antenna in proximity to the body. As with all antennas, the performance of ESAs is subject to fundamental trade-offs between size,

© The Author(s), 2026. Published by Cambridge University Press in association with The European Microwave Association. This is an Open Access article, distributed under the terms of the Creative Commons Attribution licence (http://creativecommons.org/licenses/by/4.0), which permits unrestricted re-use, distribution and reproduction, provided the original article is properly cited.

efficiency, and bandwidth. Therefore, optimization of efficiency should be considered as one of the main targets for antenna designs intended for wearable/on-body applications.

Reconfigurability for ESAs introduces a few additional challenges, which may typically not be evident in larger designs. An inherent requirement is the additional physical area to integrate the required components and bias network needed for reconfiguration. Compared to electrically large antennas, the impedance of ESAs is often highly frequency dependent, typically exhibiting small resistance and a large reactance. This may negatively affect the overall performance when applying certain tuning mechanisms [9]. Current research in reconfigurable ESAs is heavily focused on frequency, pattern, or polarization reconfigurability [10, 11]. In prior investigations on wearable ESAs (see, e.g., [12]), additional practical limiting factors have not been comprehensively considered, which typically include: (i) the need for frequency reconfigurability in the different 5G NR bands, (ii) satisfactory on-body operation in terms of total efficiency, and (iii) simultaneous adherence to strict space constraints. Nonetheless, several state-of-the-art and partially comparable ESAs presented in [11, 13–17] are benchmarked against the proposed work in Section III-D.

This paper presents a band-switchable ESA for application in a wearable electrocardiogram (ECG) monitoring device. Due to the limited size for integration into the device, its practical feasibility in terms of resonance, radiation, and operation has been preliminarily investigated in our previous work [18], to which this paper is an extension. The proposed antenna operates at 875–934 MHz, denoted as the low band (LB), and at 1.72–2.2 GHz, denoted as the high band (HB). The antenna is designed based on a multi-resonance topology consisting of feeding and shorted strips based on [19]. Despite adopting similar principles in generating resonance, the innovation in this work resulted in a footprint reduction of approximately 75% and a volume reduction of 87% compared to the originally proposed structure, while retaining operation in the sub-1 GHz band. To introduce reconfigurability, the feed line of the antenna is integrated with a switch to allow its operation in two configurations: (i) Configuration 1 (875–900 MHz), and (ii) Configuration 2 (898–934 MHz and 1.72–2.2 GHz). The antenna was optimized using electromagnetic and circuit simulations prior to prototyping and measurements, both in free space and on the body. As a final validation, the SAR is also considered and assessed. Finally, a simple solution in the form of a thin metal plate is positioned between the antenna and the user to reduce the electromagnetic coupling to the user [20].

This proposed antenna is, to the best of the authors' knowledge, highly innovative considering the size and performance, both in terms of bandwidth and on-body operation. Besides that, the antenna footprint allows the possibility to integrate other useful circuitry in the same volume. Moreover, the matching and control circuit/scheme in this work is designed to be straightforward to minimize component count and design complexity. On the contrary, comparable ESAs either may not have such strict space restrictions for the antenna (relative to overall device size) or may require operating the antenna consistently close to the body. These antennas are generally aimed at optimizing the use of available space in the device to achieve the best performance. Ultimately, it can also be observed that the proposed antenna achieves a relatively wide bandwidth despite its size being comparable to state-of-the-art ESAs (see footnote 2 in Table 2).

The rest of the paper is organized as follows. Section II will first present a calculation of the antenna requirements based on the device size limitations and the classical Chu limit [21] for defining an ESA. Then, Section III discusses the design step and methods used to gain the most performance out of the design. After that, the measurement setup and results are presented and analyzed in Section IV. Lastly, the design is benchmarked against several comparable designs prior to the concluding remarks.

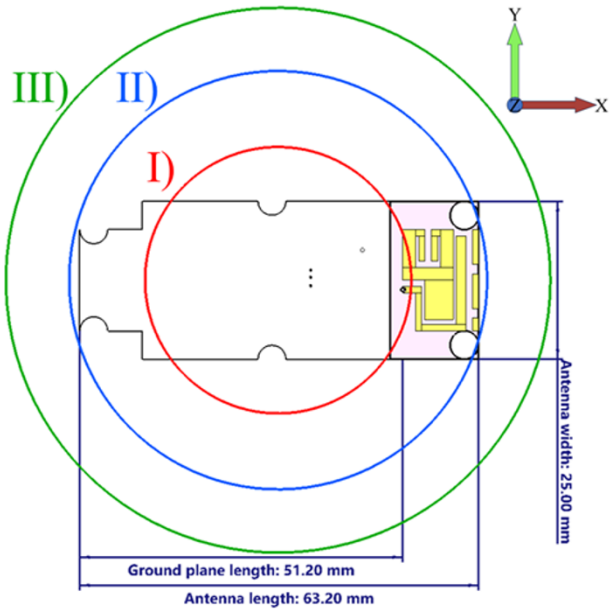


Figure 1. Visualization of the different enclosing spheres with radius a according to (1). Area allocated for the antenna design is highlighted in pink. The major dimensions of the PCB are annotated.

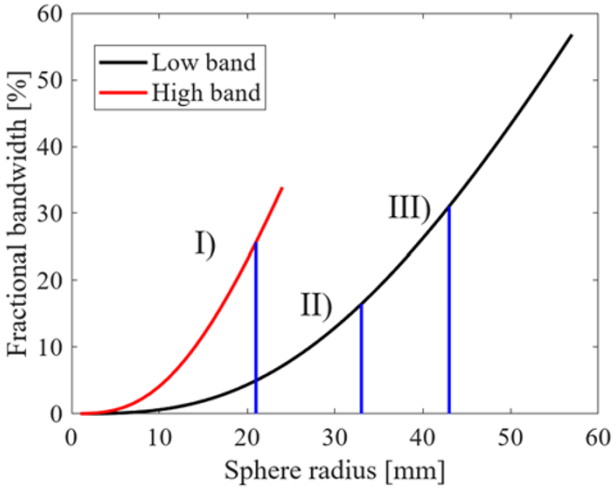


Figure 2. ESA bandwidth limits calculated using eq. (1) in comparison to the enclosing sphere radius a. The markers indicate the following cases: I) Size required for high-band operation: $a = 21$ mm / $Bw = 26\%$. II) Size of the design: $a = 33$ mm / $Bw = 16\%$. III) Size required for low band operation: $a = 43$ mm / $Bw = 31\%$.

Reconfigurable ESA system

Principle of electrically small antennas

According to the definition, the size of an ESA is much smaller compared to the wavelength λ and can be defined as [22]:

$$ka = \frac{2\pi}{\lambda}a < 1, \tag{1}$$

https://doi.org/10.1017/S1759078726103225 Published online by Cambridge University Press

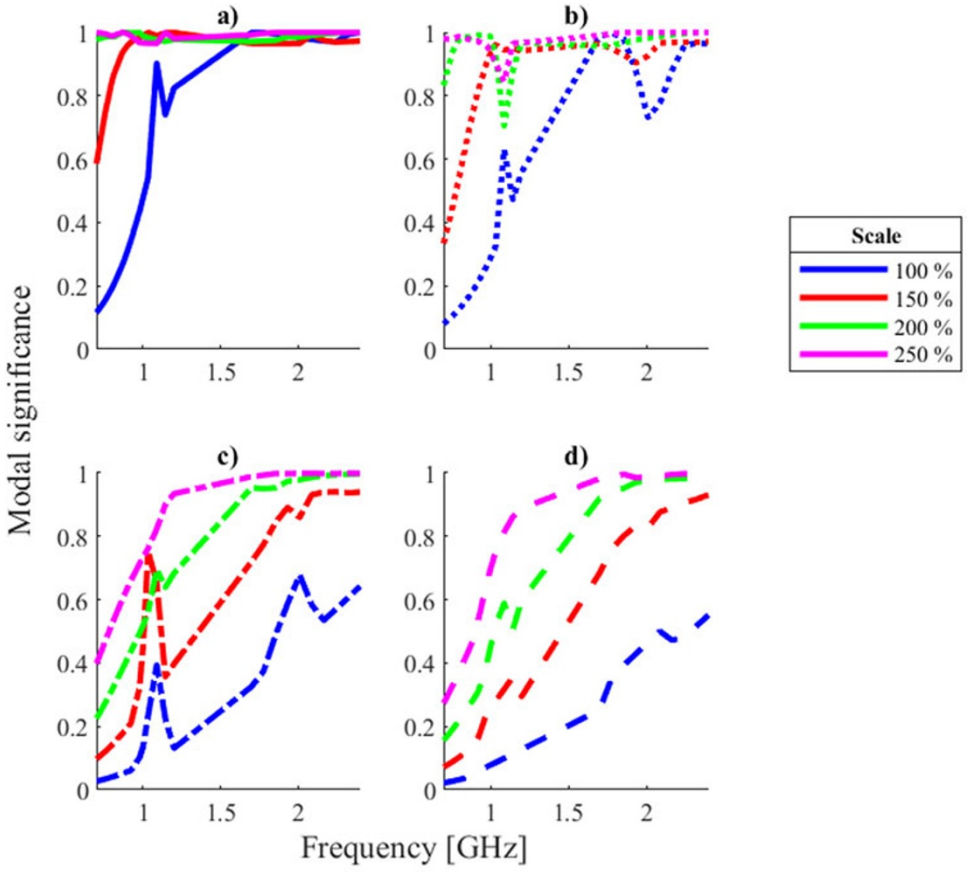


Figure 3. The change in modal significance of the first four characteristic modes at 900 MHz: a) Mode 1, b) Mode 2, c) Mode 3, and d) Mode 4, when the ground plane size is increased. The size of the ground plane (white) in Figure 1, was increased by 50% (red), 100% (green), and 150% (magenta), in both the *x* and *y* directions, whereas (blue) is the reference size. The different mode currents can be seen in Figure 4.

where a is the radius of a sphere (also called the radiansphere) enclosing the antenna, and k is the wavenumber. Based on (1), the equation defining the fractional bandwidth (B_{frac}) of the antenna is:

$$B_{\text{frac}} = \frac{S-1}{Q_{\text{min}}\sqrt{S}}, \tag{2}$$

where S is the standing wave ratio and the minimum Q value (Q_{min}) is:

$$Q_{\text{min}} = (ka)^{-3} + (ka)^{-1}. \tag{3}$$

This expression is the well-known Chu–Harrington limit [21, 23, 24].

In this work, a challenging set of limits has been defined for the antenna due to the compactness of the device, as shown in Fig. 1. Different spherical radii calculated using (1)-(3) are visualized in the two-dimensional xy plane, and the area allocated for the antenna placement is highlighted in pink. Note that the vertical area of the spheres cannot be utilized due to the geometrical constraints of the device. On the other hand, the expected fractional bandwidth (Bw) limitations for the radii of Fig. 1 are plotted in Fig. 2. When estimating the Bw, the low band frequency is calculated based on $S_{lb} = 3$ at $f = 830$ MHz, and the high band case uses $S_{hb} = 2$ at $f = 1.95$ GHz. The plotted red and black lines in this figure highlight the electrically small regions for the high and low bands, respectively. It is worth noting that the ESA limit in the high band is at $a = 24$ mm, which is slightly smaller than the size of the design. Despite not being considered electrically small at the high band (with $ka_{hb} = 1.35$), a contrary and challenging condition exists at the low band (with $ka_{lb} = 0.57$).

Due to the narrow bandwidth available from ESAs, achieving instantaneous and wide bandwidth is very challenging. To widen bandwidth, multiple resonating structures that operate in complementary, closely-spaced bands could be implemented, similar to the technique in [25]. However, due to the limited space available in this device, such a technique is not a viable option. Instead, enabling multiband operation using a switching element is a more realistic alternative. Switches do not require a large footprint, but enable the switched operation of the antenna resulting from multiple matching networks [17]. This, in turn, allows the antenna to operate over the wider targeted bandwidth of operation when switching across closely-spaced bands. In this paper, the number of states is kept small (two) to keep the control circuitry manageable.

In practice, the band-switchable antenna system is a concept intended for the Bittium Faros$^{\text{TM}}$ series of wearable cardiac monitors [26]. This requires the antenna section to be accommodated in an area of $14\times25\,\text{mm}^2$ ($0.04\times0.07\lambda^2$) (area highlighted in pink). Besides that, it is assumed that the feed line and lumped components will be integrated within the same area as other circuits (printed circuit board areas in white in Fig. 1). These aspects will be explained in more detail in the following subsections.

https://doi.org/10.1017/S1759078726103225 Published online by Cambridge University Press

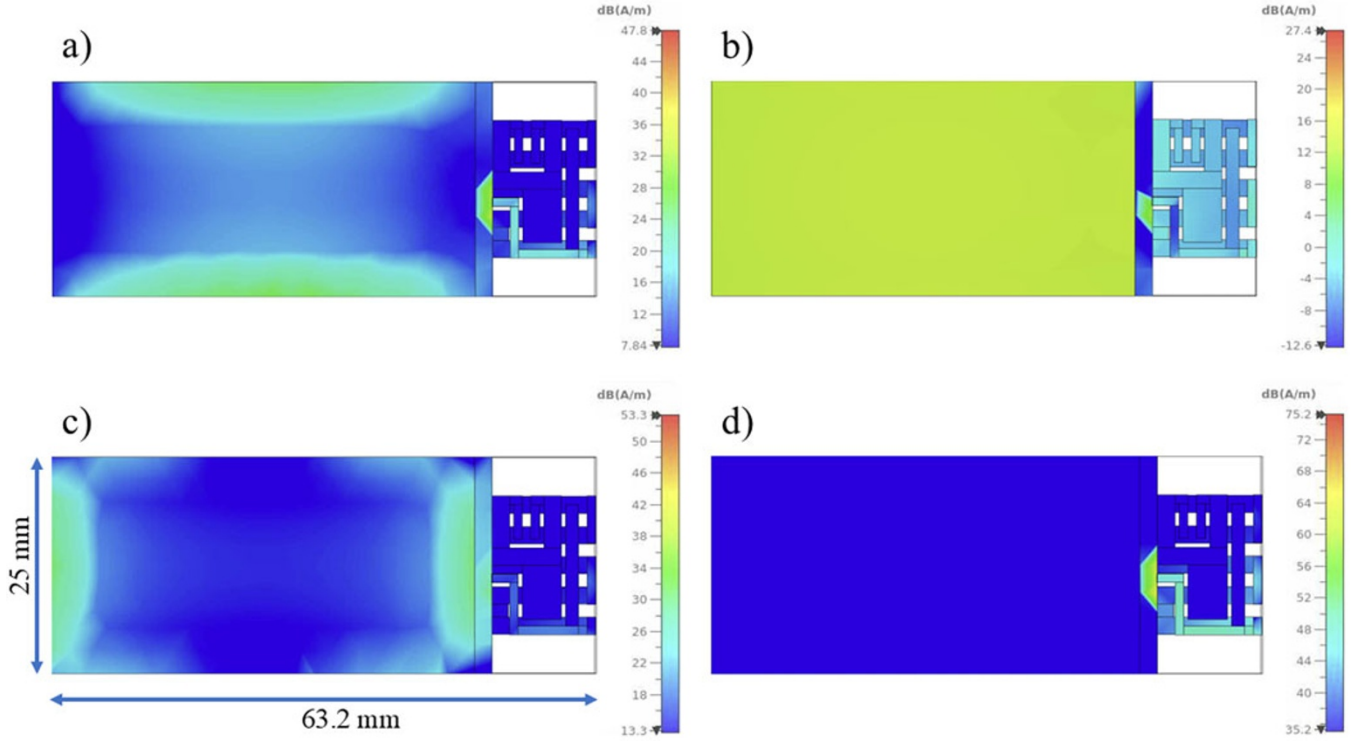


Figure 4. The surface currents at 900 MHz for the four modes shown in Figure 3: a) Mode 1, b) Mode 2, c) Mode 3, and d) Mode 4. The orientation is similar to the model in Figure 1.

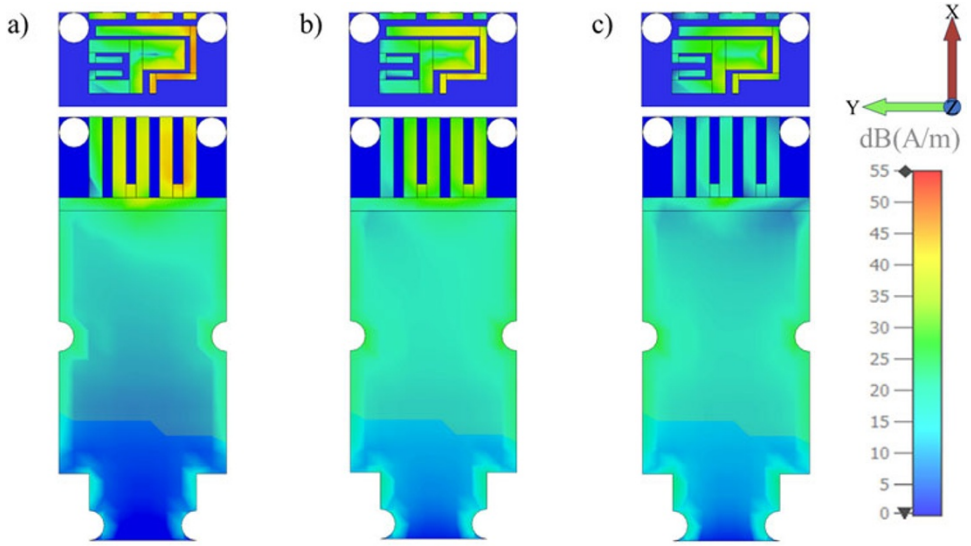


Figure 5. Maximum current distribution at a) 936 MHz, b) 1.76 GHz, and c) 2.06 GHz. Both sides of the antenna are shown.

Characteristic mode analysis

Characteristic mode analysis is an efficient tool to analyze the potential performance of an antenna design. It provides insight into the possible modes excited on a structure at a given frequency, allowing a more analytical path to identify the most suitable feed locations [27, 28].

To have an initial idea of the potentially available characteristic modes from the structure based on the lowest targeted frequency of 900 MHz, a series of characteristic mode analyses is first performed with varying ground plane sizes. When the ground plane is scaled to 150, 200, and 250% of the nominal size, the size of the antenna element remains constant in all cases. The modal significance of the first four characteristic modes at 900 MHz, when the ground plane size is increased in both axial dimensions (x and y), is shown in Fig. 3. It can be observed that the set physical size limitation (100%) of the device significantly restricts the availability of significant modes for antenna radiation. As the device size is

https://doi.org/10.1017/S1759078726103225 Published online by Cambridge University Press

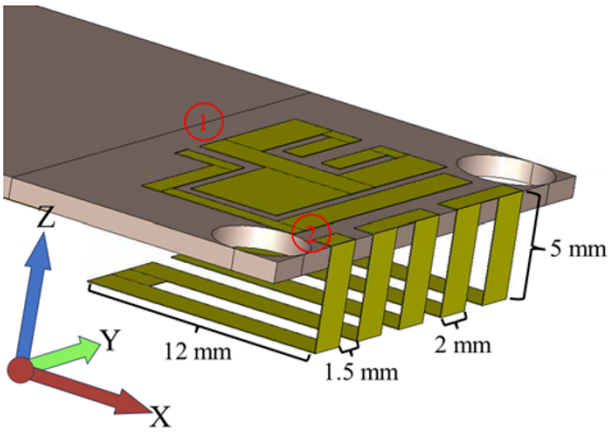


Figure 6. Meanderline structure with dimensions. 1) The feed location and 2) the aperture tuning component location.

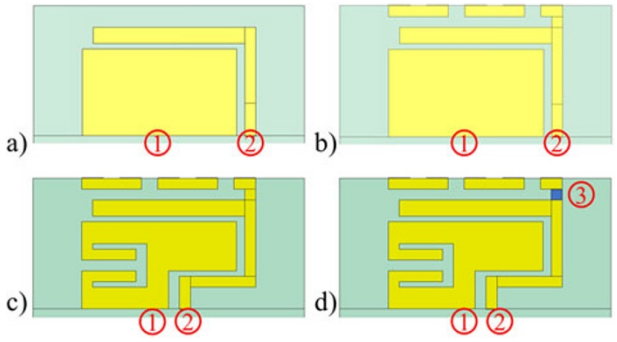


Figure 7. The different radiating structures, for which $|S_{11}|$ results are shown in Figure 8: a) Grounded strip and simple patch, b) added meander line, c) modified patch, and d) additional aperture tuning inductor (2.2 nH, same as in the final structure of Figure 6). Here, (1) marks the feed port, (2) marks the grounding, and (3) marks the placement of the aperture tuning inductor.

increased, more modes become significant at the lower frequencies, with selected modes retaining their operation at the 1.7 GHz band.

Next, based on the 100% ground plane size limitation (blue line in Fig. 3), the corresponding surface currents generated by different modes are investigated at 900 MHz. The results are illustrated in Fig. 4. Mode 1 in Fig. 4(a) has current flowing at the edges of the major axis, whereas for Mode 2 shown in Fig. 4(b), the main current is distributed evenly and directed along the minor axis. On the other hand, the currents of Mode 3 depicted in Fig. 4(c) are also directed along the minor axis, but the flow is mainly at the edges of the ground plane. The fourth highest modal significance, mode 4 in Fig. 4(d), has no current in the ground plane and a relatively high activation frequency. Based on this, it can be concluded that the antenna element as a standalone structure does not produce significant radiation performance for this design, but requires the ground plane to be excited to achieve reasonable performance. This kind of operation is similar to capacitive coupling element (CCE) based handset antennas [29]. Due to the strict size requirements of the device, the design is kept in the set limits and not increased from 63.2×25 mm^2.

Figure 5 shows the current distribution for three different frequencies. From these, we can analyze how the different parts of the design affect the performance of the design. In Fig. 5(a), it can be seen that there is a high current in the shorted section. As seen in Fig. 4(a), the strongest characteristic mode also has the same strong current in the shorted strip. There is also a relatively high current in the meander line that reduces as the frequency increases.

The current in the ground plane stays in the same range regardless of the frequency, with slight deviations as the characteristic modes change. For the 1.76 GHz current distribution, the horizontal section before the meander line and the meander line itself have higher current flows compared to the 2.56 GHz case. These are also important for the operation at the high band. The actual antenna element has quite a stable excitation through all the different frequencies. As a conclusion, all of the parts from the design play a crucial role in the achieved performance, with the ground plane being the limiting factor for achieving a lower frequency.

Antenna design and aperture tuning

The antenna design is modified from the design presented in [19] with more challenging space requirements. The unique goal is to retain most of the bandwidth in the LB and maintain the operation in the HB despite this space limitation. The design consists of a U-shaped feeding strip and two sections of shorting strips. The two sections of the shorting strips are connected using an inductor. The first part of this shorting strip is placed on the same PCB layer as the feeding strip, whereas its second part is bent in a meandered form inside the 3D-printed casing of the device. To enable more precise impedance tuning, the antenna aperture is tuned by an inductor (denoted by circle no 2), as shown in Fig. 6. The grounded meander line acts as an extension to the ground plane of the PCB, having the electrical length extended with the aperture tuning inductor [30]. Such method maintains design simplicity and avoids the need for inductance tuning using complex geometrical modifications due to space limitations.

Antenna simulations and optimization are performed using CST Microwave Studio Suite 2023, whereas optimization for the matching circuit is performed using Optenni Lab software [31]. The reconfigurable antenna system is designed on a cost-efficient, 1-mm thick FR4 substrate ($\varepsilon_r = 4.3$ and metal thickness of 18 μm). The PCB is housed in a 3D-printed case, with an area of 66×33 mm^2 and which lifts the PCB 10 mm from the bottom to allow placing the meander line below the PCB.

Antenna operation

The initial design consists of a patch-like structure, feed position, and the grounded segment is denoted with 1 and 2, respectively, in Fig. 7. This provides the basis for the high-band operation of the structure, with the grounded segment being observed to significantly contribute to this behavior. The effect of the ground extension and aperture tuning from Fig. 7 is shown in Fig. 8.

When adding the meander line structure, which extends below the ground plane of the PCB, as shown in Fig. 7(b), a new resonance appears at the low band. This modification also slightly boosts the high-band operation. In Fig. 7(c), the patch is modified to its final form by introducing a T-shaped cutout and moving the grounding point of the shorted strip. With this modification, the high-band performance is again slightly improved, and the low-band resonance shifts down in frequency.

To further tune the low-band operation, a discrete inductance (2.2 nH) is added between the grounded segment and the meander line. This shifts the low-band resonance toward the target range,

https://doi.org/10.1017/S1759078726103225 Published online by Cambridge University Press

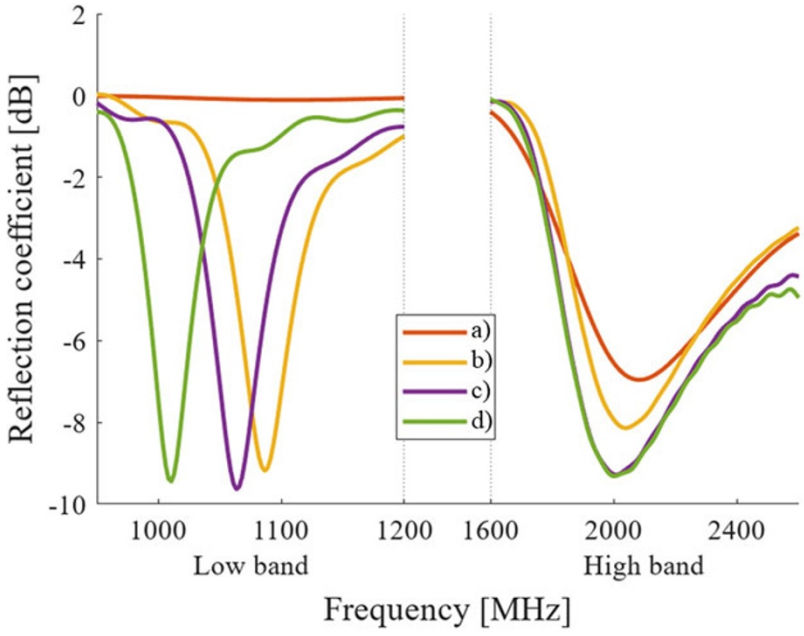


Figure 8. The effect of the different antenna parts on the input reflection coefficient ($|S_{11}|$). The different design stages are visualized in Figure 7. The parts are not optimized for free-space operation; thus, the actual performance in this figure should only be regarded as a comparison between the accompanying results.

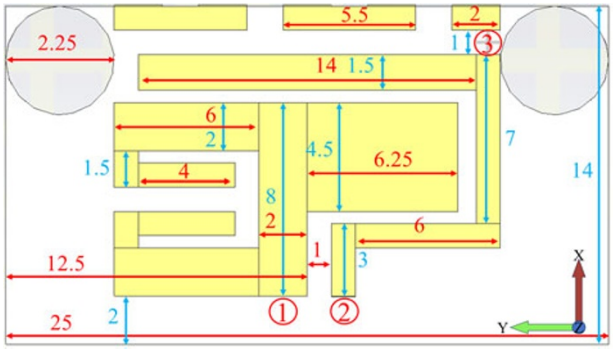


Figure 9. Top view of the antenna element with dimensions annotated in mm. (1) Marks the feed location, (2) marks the grounding, and (3) the aperture tuning component location.

with the amount of frequency shift defined by the additional inductance value. It can be observed that the higher the inductance value, the lower the frequency shifts. However, this comes at the cost of decreased total efficiency, and a proper evaluation of the trade-offs is required.

Antenna input matching

To further improve the antenna input impedance matching (to 50 Ω) in the low band, lumped matching elements are used due to their compact size compared with that of the antenna. Besides that, these components also allow frequency tunability with a switching network.

The radiating structure is shown in Fig. 9. It is designed in a switchable format to operate in two segments in the low band, using Configurations 1 (875–900 MHz) and 2 (898–934 MHz). In Fig. 10, the RF input is fed by an SMPM connector (Rosenberger) to a switched matching network. This network is switched between the two configurations using a simple combination of an inverter (Rohm) and a mechanical switch (Wurth) as a proof-of-concept. The matching networks are located between RF switches (Qorvo). The matching network for Configuration 1 consists of a parallel capacitor (Murata 5.7 pF) and a series inductor (Murata 6 nH). For Configuration 2, a simple series capacitor (Murata 3.3 pF) is used.

Results and discussion

Measurement setup and body phantom

The optimized design was then fabricated, as shown in Fig. 11. *S*-parameter measurements were performed using an HP 8720ES vector network analyzer (VNA), whereas radiation patterns and efficiency were assessed using a SATIMO Starlab measurement system, as seen in Fig. 12. *S*-parameter measurements were performed on a homogeneous body phantom whose dimensions are $18\times24\times15$ cm^3. The size of the phantom was then reduced to $10\times20\times8$ cm^3 for the measurements of radiation pattern and efficiency due to the space and weight constraints on the antenna measurement platform. The simulated phantom shares the dielectric properties of the *Basic phantom* design of [32], and the phantom for measurements was made to match the same model using the recipe/part of the same recipe as the body model in [33]. An RF cable and an SMPM-to-SMA adapter are used throughout the measurements.

On-phantom measurements were performed using a 10 mm thick piece of Rohacell foam spacer, as seen in Fig. 13. The spacer is emulating the on-body adapter, which is included in the Bittium Faros^{TM} device [26]. Under the spacer, a piece of copper tape was used in on-body results as a reflector, as seen in Fig. 14, to reduce SAR, with a size roughly matching the size of the device [20].

Free space performance

Scattering parameters

Figure 15 presents the simulated and measured free space reflection coefficient for the antenna system. There is a slight shift upward in the measured resonant frequency in the low band and significant dampening in the matching compared to simulations. The high

https://doi.org/10.1017/S1759078726103225 Published online by Cambridge University Press

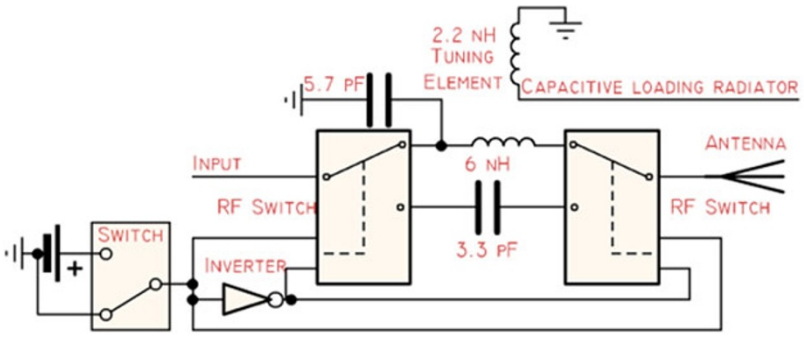


Figure 10. Schematic of the matching- and control-circuit, with the used components annotated.

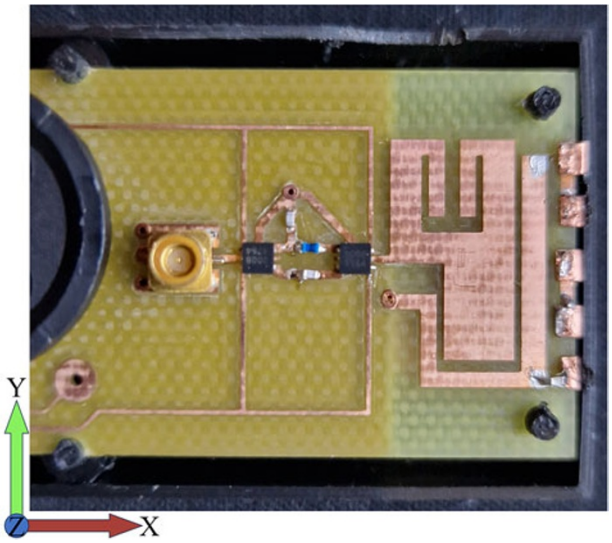


Figure 11. Close-up of the fabricated design, with the matching circuit and RF input.

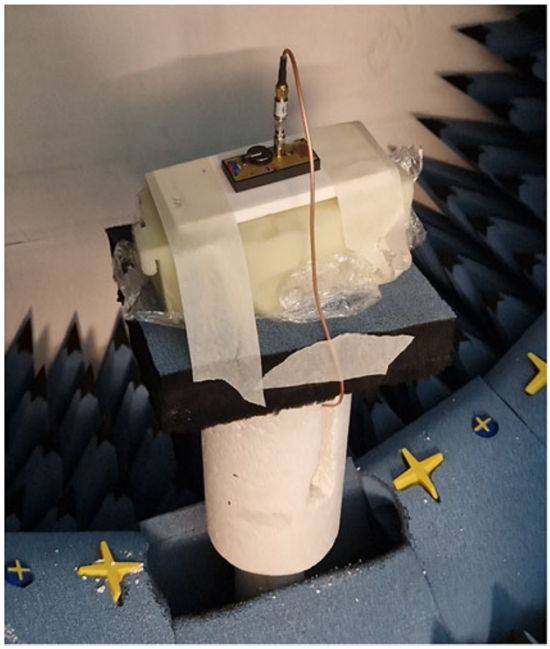


Figure 12. The reduced body phantom ($10\times20\times8\,\text{cm}^3$) setup in the Satimo Starlab, for efficiency and gain measurements.

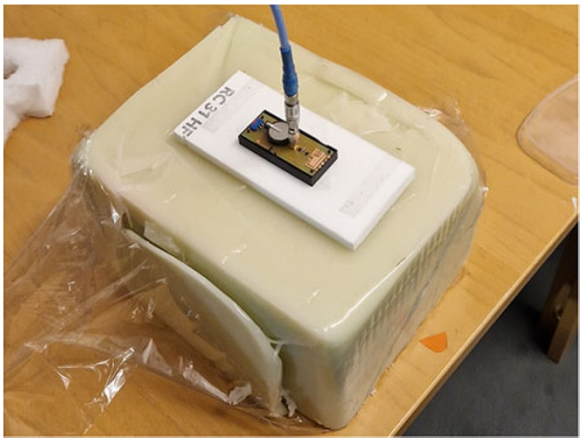


Figure 13. On-body S-parameter measurements, with a $18\times24\times15\,\text{cm}^3$ body phantom.

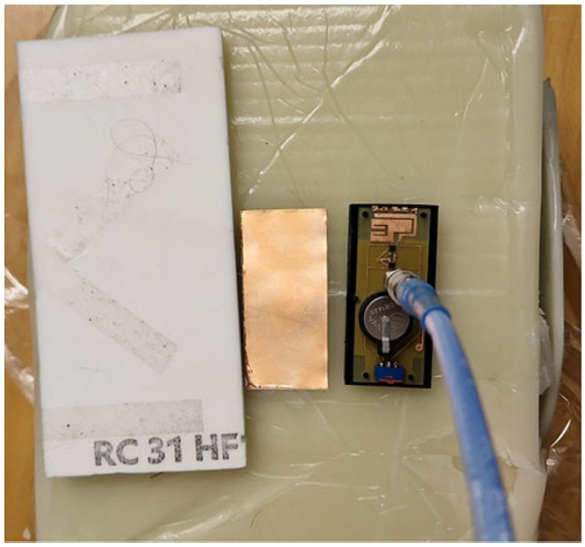


Figure 14. The Rohacell spacer and copper tape reflector next to the antenna.

band displays an opposite behavior, with the measurement having a higher peak in the matching and the resonance in a slightly lower frequency, although the high band retains the required bandwidth.

https://doi.org/10.1017/S1759078726103225 Published online by Cambridge University Press

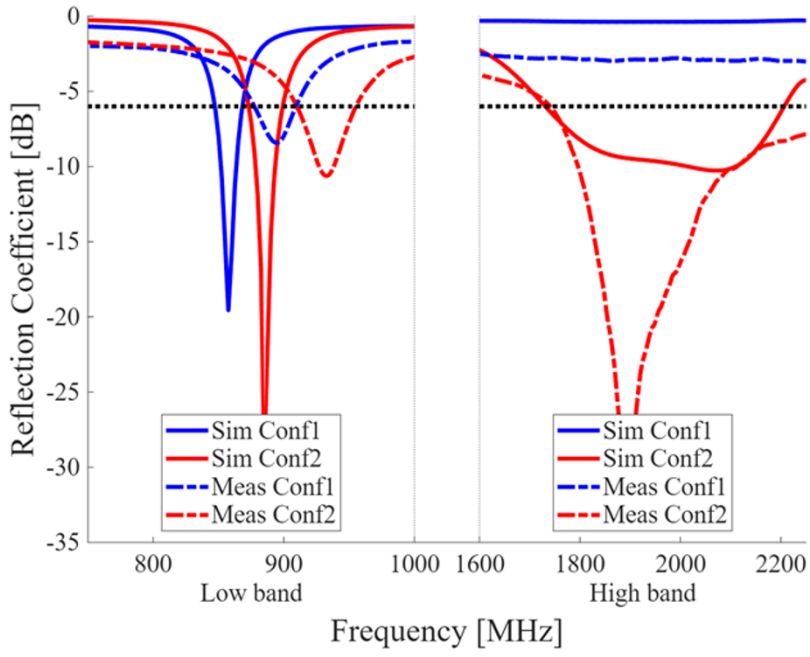


Figure 15. Simulated and measured reflection coefficient of the antenna in *Free space*. Here, *Conf1* and *Conf2* refer to the different matching network configurations.

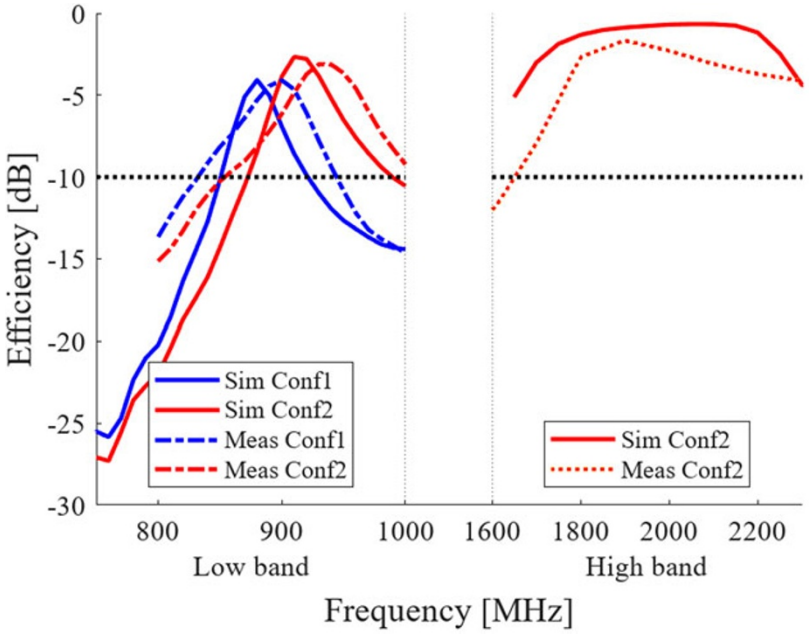


Figure 16. Simulated and measured free space total efficiency of the antenna.

Efficiency

Figure 16 shows the total efficiency of the antenna in free space. The efficiency peaks are around 0.9 GHz (−4 dB), 0.93 GHz (−3 dB), and 1.9 GHz (−2 dB), which align well with the deepest resonances in the reflection coefficient of Fig. 15. A higher efficiency would be preferable, but ESAs have naturally low efficiency [7]. Although the measured reflection coefficient has a deeper notch at the high band compared to the simulation, the efficiency does not exhibit the same behavior. This is likely due to additional losses in actual components, which lower the peak efficiency of the prototype.

Radiation patterns

In Fig. 17, the simulated and measured gain is plotted for the free space case. The low band gain is slightly below 0 dB with deviation to as low as -10 dB, with a mostly omnidirectional pattern. The high band is similar with a deviation at $\phi = 90^\circ$ and $\theta = 120^\circ$ in Fig. 17(d).

On-body performance

This subsection describes the on-body measurements and their results. The body phantom is described in Section III-A. with the general measurement setup.

Scattering parameters

The simulated and measured on-body reflection coefficients are shown in Fig. 18 for both switch configurations. The combined −6 dB bandwidth are from 875 MHz to 934 MHz in the low band,

https://doi.org/10.1017/S1759078726103225 Published online by Cambridge University Press

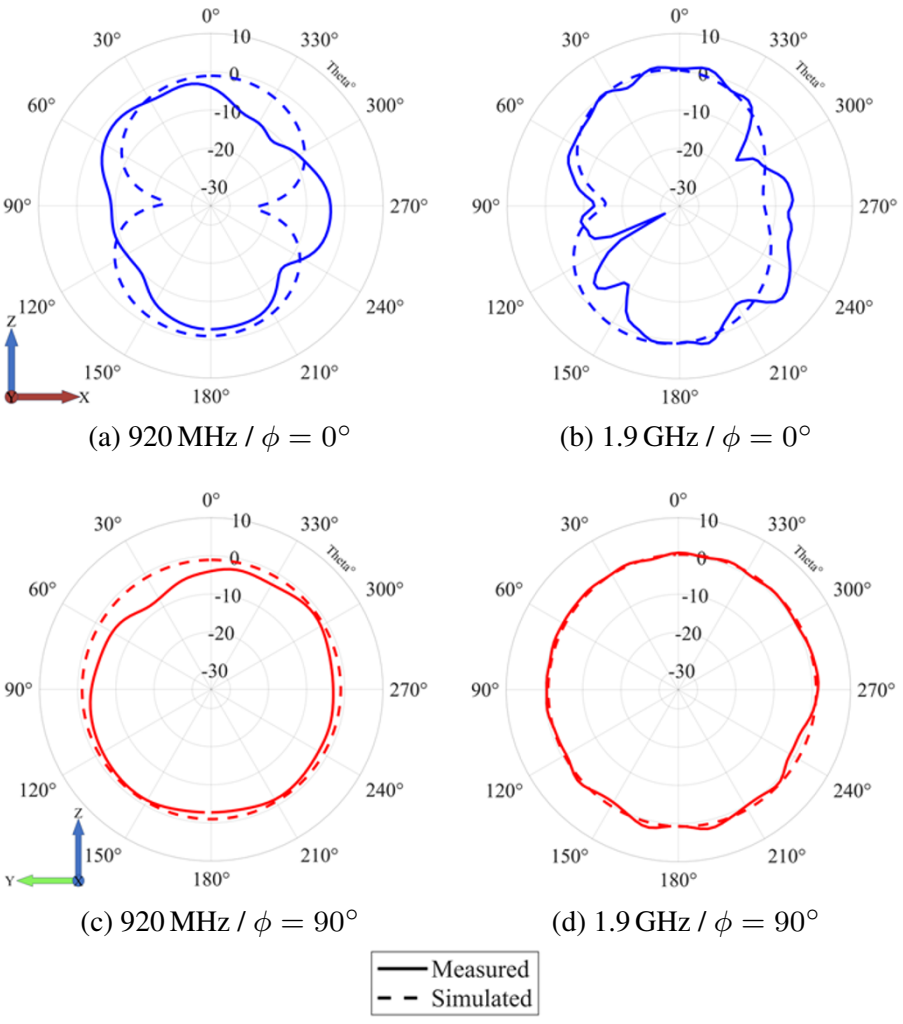


Figure 17. Simulated (dashed) and measured (solid) free-space radiation patterns at: (a) 920 MHz, $\phi = 0°$ cut, (c) 920 MHz, $\phi = 90°$ cut, (b) 1.9 GHz, $\phi = 0°$ cut, and (d) 1.9 GHz, $\phi = 90°$ cut. The orientation of the antenna can be seen in Figures 1 and 11. a) 920 MHz / $\phi = 0°$. b) 1.9 GHz / $\phi = 0°$. c) 920 MHz / $\phi = 90°$. d) 1.9 GHz / $\phi = 90°$.

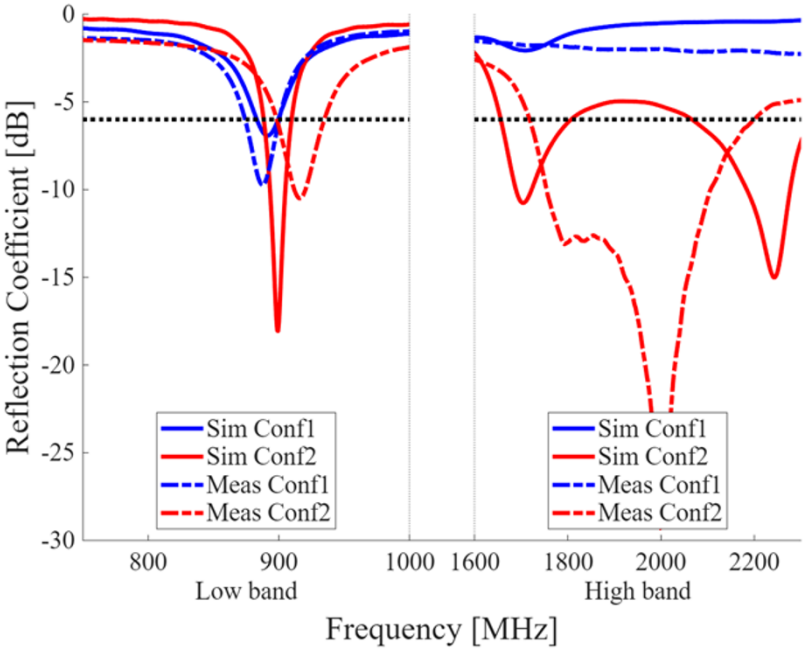
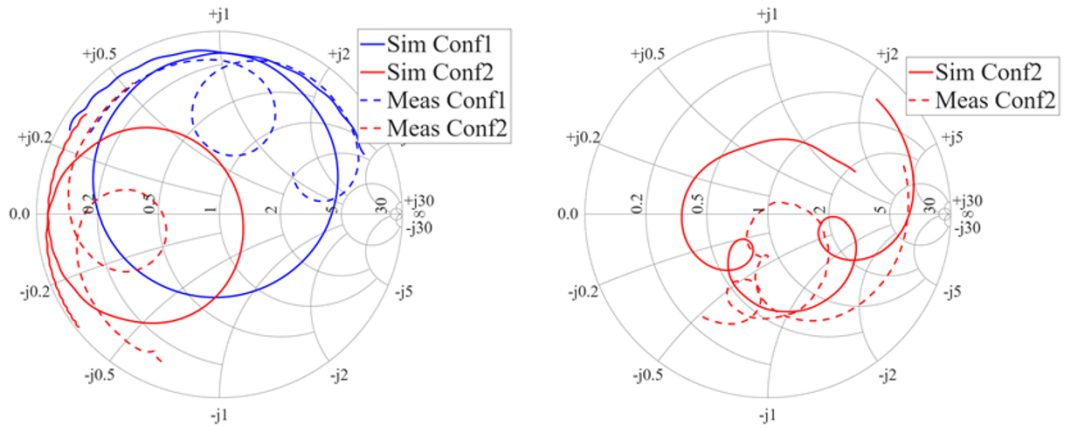


Figure 18. Comparison of simulated and measured on-body reflection coefficients. Bandwidth is defined according to the –6-dB matching criterion (indicated by the black dotted line).

https://doi.org/10.1017/S1759078726103225 Published online by Cambridge University Press



(a) Low band: 0.6–1.2 GHz (b) High band: 1.5–2.5 GHz

Figure 19. Comparison of simulated and measured complex reflection coefficients. a) Low band: 0.6–1.2 GHz. b) High band: 1.5–2.5 GHz.

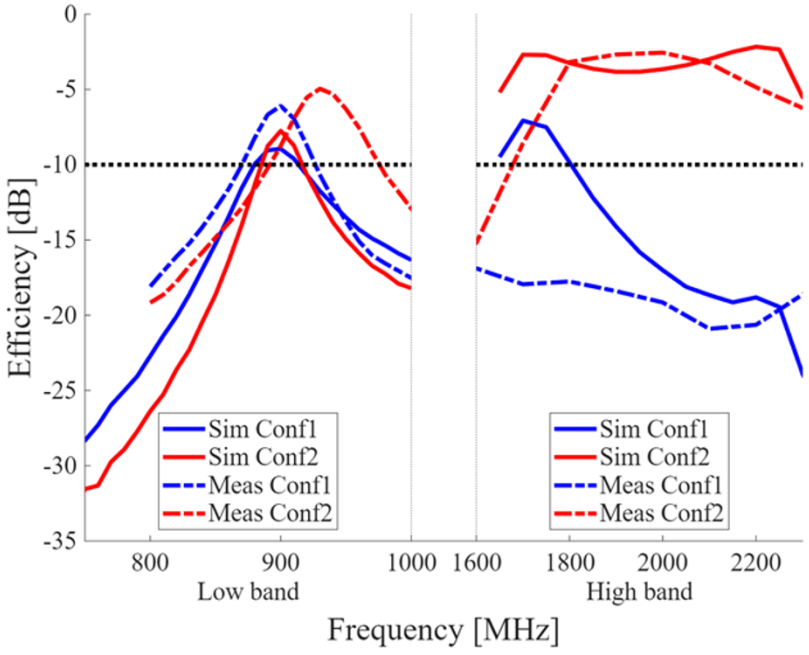


Figure 20. Comparison of simulated and measured on-body total efficiency. The black line marks the –10 dB line used to determine the efficiency bandwidth.

and from 1.7 GHz to 2.2 GHz in the high band The simulated low-band resonances are clearer (with significantly deeper dips) and a gap between the two configurations. In the high band, there is a more noticeable difference between the simulated and measured results relative to their performance in free space. Although both curves exhibit a dual-resonance response when operated in proximity to the body phantom, a larger gap between the two resonance peaks is observed in simulations.

The measured on-body bandwidth in the low band (875–934 MHz) is slightly wider than the simulated one (886–910 MHz) and covers the entire target frequency range. In the high band, the measured on-body results featured a bandwidth of 1714–2190 MHz, which almost satisfies the required bandwidth specifications. A larger discrepancy is seen in the high band due to the practical differences in the properties (relative permittivity and conductivity) of the phantoms across frequency. The properties of the phantom model used in simulations are extrapolated across the frequency of interest, whereas the properties of the fabricated phantom can be made close to the required values using the current manufacturing method in either the low or high band only. In this case, considering the more sensitive behavior of the antenna performance in the low band due to the larger distance needed to decouple them, the phantom has been fabricated based on the properties in this (low) band to evaluate the worst-case performance scenario of on-body coupling. Besides that, unlike in simulations, it is challenging to ensure that the fabricated phantom produces exact same homogeneous permittivity and conductivity in practice. Variation of these properties across the phantom's width and length may occur and affect the accuracy of the measurement results. Despite these uncertainties, it is observed that the simulated and measured $|S_{11}|$ in the high band exhibited similar bandwidths, with differences mainly observed in the depths of the resonances.

In Fig. 19(a), the low band curves show that the simulated results are overcoupled, while the measured results are undercoupled. On the other hand, in Fig. 19(b), the simulated

https://doi.org/10.1017/S1759078726103225 Published online by Cambridge University Press

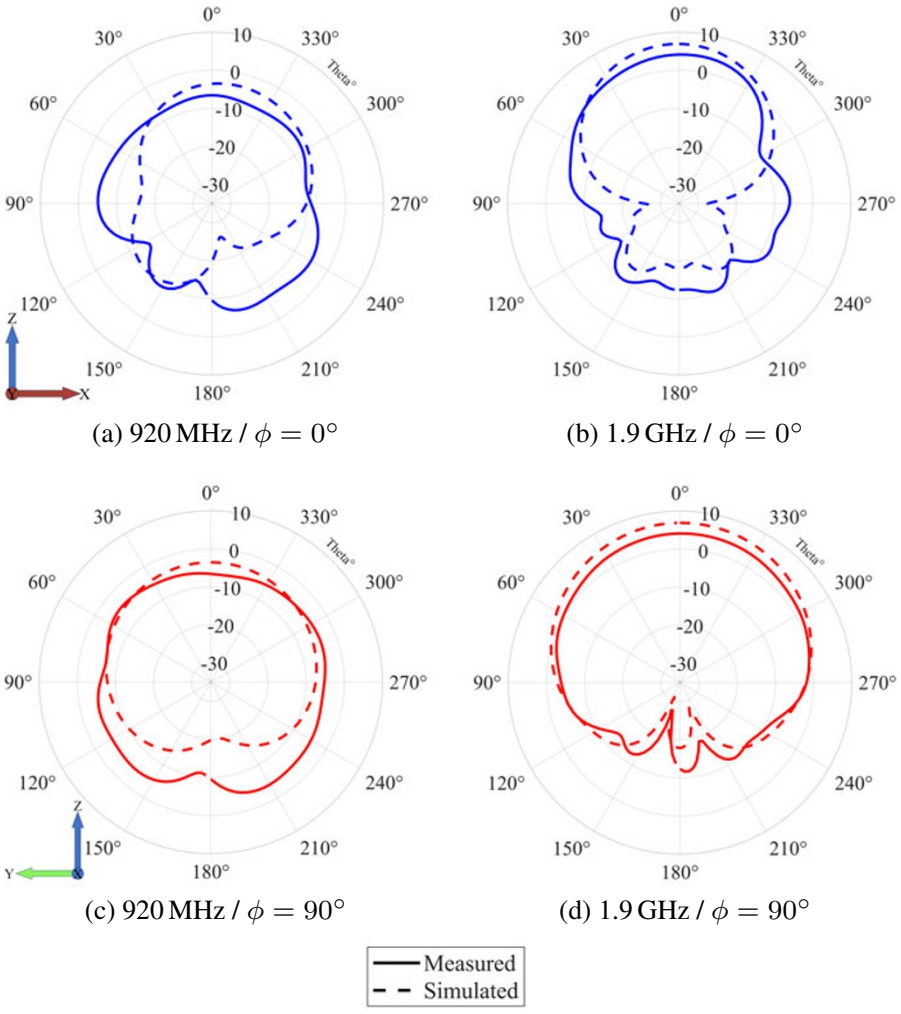


Figure 21. Simulated (dashed) and measured (solid) on-body radiation patterns at: (a) 920 MHz, $\phi = 0°$ cut, (c) 920 MHz, $\phi = 90°$ cut, (b) 1.9 GHz, $\phi = 0°$ cut, and (d) 1.9 GHz, $\phi = 90°$ cut. The orientation of the antenna can be seen in Figures 1 and 11. a) 920 MHz / $\phi = 0°$. b) 1.9 GHz / $\phi = 0°$. c) 920 MHz / $\phi = 90°$. d) 1.9 GHz / $\phi = 90°$.

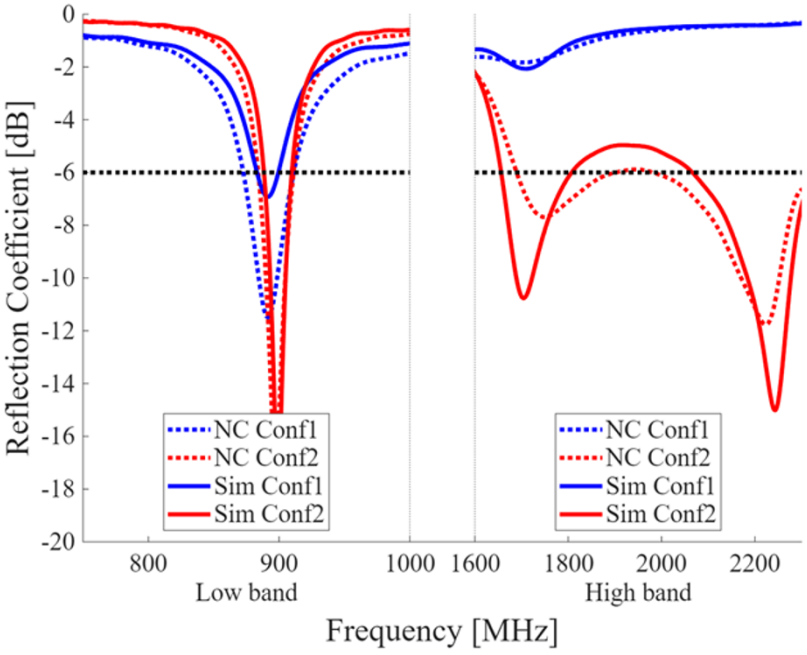


Figure 22. Simulated reflection coefficient with (Sim) and without (NC) the SAR reduction layer. Both of the results employ a 10 mm gap between the model and the phantom.

https://doi.org/10.1017/S1759078726103225 Published online by Cambridge University Press

Table 1. Simulated SAR results with an accepted power of 23 dBm and when averaging over a 1-g mass of tissue

SAR results (W/kg)	Configuration 1	Configuration 2
Low band (resonance)	0.433 (0.910 GHz)	0.379 (0.923 GHz)
High band (1.9 GHz)	0.461	0.246

high band results are undercoupled, whereas the measured results are almost critically coupled. When considering the high band results, the two simulated resonances of Fig. 18 are clearly visible as separate loops, whereas the measurements show a nascent dual resonance. Based on these observations, moving the impedance at the two resonances closer to the center of the Smith chart allows improvement of the overall matching level across the high band.

Efficiency

The efficiency simulation uses the smaller body phantom due to the reasons mentioned in Section III-A. The total efficiency of an antenna refers to the power fed to it compared to the power radiated, accounting for all losses along the signal path. In this work, a total efficiency of at least −10 dB is desired throughout the operating frequency band. Results illustrated in Fig. 20 in both the low and high bands indicate that the total efficiencies correspond well to the reflection coefficient results, and the −10 dB target efficiency is achieved over the entire −6 dB bandwidth.

Compared to the free space efficiency in Fig. 16, only a drop of −2 dB is observed when the body phantom is introduced. This effect is contributed by the existence of the reflecting copper plate, and is also comparable to the study in [8]. The difference between the low band efficiencies is a result of the lower frequency that affects the electrical size and radiation characteristics of the antenna.

Radiation patterns

The current ESA system is intended to be used on the body to collect ECG-based health information and channel it to a base station. Therefore, in this application, the antenna radiation patterns need to be designed appropriately, with the main beam pointing away from the user. At the same time, the existence of the ground plane will ensure that the performance of the antenna is not easily influenced by the coupling to the body. Moreover, high back radiation can increase SAR levels, and this should be avoided.

Prior to the on-body radiation pattern measurement, the size of the body phantom was reduced (from $18\times24\times15\,\text{cm}^3$ to $10\times20\times8\,\text{cm}^3$) to comply with the mechanical rotation of the StarLab measurement system. Nonetheless, it is expected that this change will have minimal effects in evaluating the true performance of the antenna on the body, as the distance from the edges of the antenna to the edges of the body model is at least 0.1λ. In Fig. 21, the gain patterns for the design are shown, for both the low band (920 MHz) and the high band (1.9 GHz), on two different axes. The gain toward the body is significantly increased in measurements in the low band, as seen in Fig. 21(a) and (b). In other aspects, the measured gain is similar to the simulated gain. Gain simulations were also performed using the smaller body phantom model.

Specific absorption rate

The SAR is a measure of power absorption in body tissue/phantom, and its limit is 1.6 W/kg averaged over a 1-g mass of tissue according to the Federal Communications Commission (FCC) standards in the United States [3]. This regulation is chosen as it is one of the strictest. In comparison, the IEEE limit is 2 W/kg averaged over 10 g of tissue, which is relatively easier to obtain.

Table 2. Comparison with other relevant work

Ref.	Band	Dimensions (mm^2)	Dimensions (λ)	BW (MHz) / (%)	f (GHz)	η_{rad}	On-body
[13]	Single	$12\times12\times\pi$	$\phi0.20$	149 (6.08%)[2]	2.45	22%	yes
[14]	Single	80×80	0.23×0.23	15 (1.7%)	0.86	NA	yes
[15]	Single	60×60	0.07×0.07	5.4 (1.5%)	0.36	7.6%	no
[15]	Single	80×90[1]	0.09×0.10	4.3 (1.28%)	0.336	1.21%	no
[11]	Single	$32\times32\times\pi$	$\phi0.20$	31 (3.26%)	0.95	77%	no
[34][7]	Low band	36×38	0.11×0.12	26 (2.84%)	0.915	62%[6]	yes
	High band	—″—	0.29×0.30	40 (1.68%)	2.38	65%[6]	yes
[16]	Low band	30×41	0.08×0.11	42 (5.3%)	0.8	33%[4]	yes
	High band	—″—	0.24×0.32	286 (12.2%)[3]	2.35	33%[4]	yes
[17]	Low band	65×70	0.15×0.16	262 (32%)[2]	0.83	32.4%[5]	no
	High band	—″—	0.37×0.40	460 (24%)[2]	1.94	58.4%[5]	no
This work	Low band	25×63.2	0.08×0.19	59 (6.56%)[2]	0.9	32%[6]	yes
	High band	—″—	0.16×0.39	480 (24.5%)[3]	1.96	61%[6]	yes

[1]With a 150×140mm^2 ground plane.
[2]–6dB bandwidth, compared with –10dB bandwidth.
[3]The high band cannot be considered as electrically small.
[4]With 12mm to the phantom.
[5]Averaged total efficiency.
[6]Total efficiency.
[7]Two bands at higher frequencies not reported here.

https://doi.org/10.1017/S1759078726103225 Published online by Cambridge University Press

In this work, the SAR for the band-switchable ESA system is simulated in CST using a homogeneous body phantom. An accepted power of 23 dBm was used to roughly match a possible use case power. A 10-mm gap is chosen to emulate the spacing between the antenna and human body in an actual use case, which includes the ECG electrode and an adapter for the device. The effect of the additional metal layer is evaluated in terms of reflection coefficients in Fig. 22. In the low band, a stronger resonance peak is seen for Configuration 1, without any obvious changes in Configuration 2. On the other hand, in the high band, a similar increase in resonance strength is noticed for the resonance peaks, resulting in a slight degradation of the reflection coefficient in the center of the whole high band. Despite this, the measured $|S_{11}|$ of the prototype with the phantom in the high band indicated satisfactory performance while producing SAR values within the accepted regulatory level.

The SAR results are shown in Table 1, indicating satisfactory compliance with the safety levels. These SAR levels can be further reduced by modifications of the transmit power duty cycle [35]. Besides that, future research could include more advanced and compact metamaterial-based solutions such as artificial magnetic conductor (AMC) reflectors [36–38] to reduce SAR levels by limiting backward radiation. However, such solutions come at the cost of a larger area requirement for their implementation, as they are typically designed in the form of an array of unit cells at their operating frequency. Considering the need for such a reflector in the low band in this case, a significantly compact AMC reflector is needed to ensure full compliance with the current operation of the health monitoring device in practice. This is certainly a challenging aspect that can be pursued in the next stage of the research. It should be noted that SAR measurements were not possible at the time of the investigation. However, considering the reasonably large safety margins from the SAR limits, it can be expected that the measured values would also fall well within the acceptable limits [39].

Comparison with the state-of-the-art

In the literature, there are only a few similar works on ESA design for on-body operation, which also include measurements. Nonetheless, several of the most relevant works are compared in Table 2. In [13], an ESA working at 2.4 GHz is introduced for hearing aid applications. The research does not focus on bandwidth enhancement, but rather on improving radiation efficiency. In [14], an ESA designed to operate in the sub-1 GHz band is proposed. The size is significantly larger, and the investigation is focused on the wearable aspect and radiation patterns. On the other hand, in [15], two designs for operation below 400 MHz are proposed. Both designs are remarkably compact compared to their frequency. However, this significantly affects the achieved bandwidth. Neither of the designs is meant for on-body use, but as a study into ESAs. Next, in [11], a Yagi-based antenna with polarization reconfigurability is introduced. This design utilizes the vertical space in the enclosing ESA sphere with a stacked design. In [34], a small wearable antenna is introduced. The achieved footprint is small, and the targeted frequency bands are narrow, but sufficient. This design also achieves good efficiency. In [17], a reconfigurable antenna system is proposed, operating from 698–960 MHz and from 1710–2170 MHz. This is achieved using a seven-state switchable matching network, enabling wide bandwidths in both frequency bands of interest with decent efficiency. However, as this method relies heavily on the ground plane, it may not be practical to achieve the targets in this work, besides not being intended for on-body use. Perhaps the most relevant comparison for this work is from [16], in which a rectangular-spiral dual-band antenna operating in similar frequencies is proposed. Moreover, the effect of the proximity to the body is studied. A major difference between that work and the proposed antenna lies in the antenna-to-ground plane size ratio, which is more restricted in this work.

Conclusion

In this work, a compact and band-switchable antenna for potential health monitoring applications is presented. Results from simulations and measurements indicate that such an ESA can be designed and operated in a switchable manner for on-body applications at 875–934 MHz and 1.7–2.2 GHz, with an efficiency above −10 dB. Considering the challenges related to the inherent theoretical limits, the operation of the proposed antenna in these bands within an extremely small footprint of $63.2\times25\ \text{mm}^2$ ($0.18\times0.07\ \lambda^2$) is a reasonable success. Ultimately, the radiation patterns and SAR results of this antenna system indicate suitability for on-body operation. An option for near-future improvement includes employing tunable capacitors and inductors for multi-state tunability. However, it should be noted that this improved flexibility in impedance tuning comes at an increased cost and design complexity.

Acknowledgements. The authors would like to thank Dr Mariella Särestöniemi for preparing the body phantom, Dr Tung Duy Phan for helping with the pattern measurements, and the staff at FabLab Oulu for their aid in manufacturing the prototype. Optenni Ltd is acknowledged for providing access to the Optenni Lab software.

Funding statement. This work was supported in part by Business Finland through the RF Sampo project (Grant no: 2991/31/2021), in part by the Research Council of Finland (RCF) through the 6G Flagship Programme (Grant no: 369116), and in part by the IEEE MTT-S Undergraduate/Pregraduate Scholarship 2023. The work of P. J. Soh was supported by the RCF's Academy Research Fellowship ULTRAGRAM (Grant no: 355643).

Competing interests. The authors declare none.

References

1. **Lehtovuori A, Ilvonen J, Rasilainen K and Viikari V** (March 2017) Single-element handset antenna design for modern smartphones: An industrial approach. In *2017 11th European Conference on Antennas and Propagation (EUCAP)*. Paris, France, pp. 2960–2963.
2. **Chen H and Zhao A** (2016) LTE antenna design for mobile phone with metal frame. *IEEE Antennas and Wireless Propagation Letters* **15**, 1462–1465.
3. Wireless devices and health concerns. https://www.fcc.gov/consumers/guides/wireless-devices-and-health-concerns.
4. **Sun H, Zhang Z, Rose Qingyang H and Qian Y** (2018) Wearable communications in 5G: Challenges and enabling technologies. *IEEE Vehicular Technology Magazine* **13**(3), 100–109. https://doi.org/10.1109/MVT.2018.2810317.
5. (2006) IEEE standard for safety levels with respect to human exposure to radio frequency electromagnetic fields, 3 kHz to 300 GHz. *IEEE Std C95.1-2005 (Revision of IEEE Std C95.1-1991)*, 1–238. https://doi.org/10.1109/IEEESTD.2006.99501.
6. (1998) Guidelines for limiting exposure to time-varying electric, magnetic, electromagnetic fields (up to 300 GHz) In *Proceedings of the International Commission on Non-Ionizing Radiation Protection (ICNIRP)*. pp. 494–522. https://www.icnirp.org/cms/upload/publications/ICNIRPemfgdl.pdf

https://doi.org/10.1017/S1759078726103225 Published online by Cambridge University Press

7. **Nepa P and Rogier H** (2015) Wearable antennas for off-body radio links at VHF and UHF bands: Challenges, the state of the art, and future trends below 1 GHz. *IEEE Antennas and Propagation Magazine* **57**(5), 30–52. https://doi.org/10.1109/MAP.2015.2472374.
8. **Hall PS, Hao Y, Nechayev YII, Alomainy A, Constantinou CC, Parini C, Kamarudin MR, Salim TZ, Hee DTM, Dubrovka R, Owadally AS, Song W, Serra A, Nepa P, Gallo M and Bozzetti M** (2007) Antennas and propagation for on-body communication systems. *IEEE Antennas and Propagation Magazine* **49**(3), 41–58. https://doi.org/10.1109/MAP.2007.4293935.
9. **Bernhard JT, Young MW and Yong S** (2013) Challenges for frequency reconfigurable electrically small antennas. In *2013 7th European Conference on Antennas and Propagation (EuCAP)*. Gothenburg, Sweden. pp. 430–431.
10. **Shi T, Wen Y, Wang HB, Tang M-C and Yuan X** (2024) Low-profile, pattern-reconfigurable, electrically small antenna based on equivalent even and odd modes. *IEEE Antennas and Wireless Propagation Letters* **23**(1), 304–308. https://doi.org/10.1109/LAWP.2023.3323459.
11. **Tang M-C, Lin Q and Ziolkowski RW** (2020) Yagi-configured electrically small antenna with quad-polarization diversity. In *2020 IEEE International Symposium on Antennas and Propagation and North American Radio Science Meeting*. Montreal, QC, Canada. pp. 1697–1698. https://doi.org/10.1109/IEEECONF35879.2020.9329817.
12. **Kumar S, Moloudian G, Simorangkir RBVB, Gawade DR, O'Flynn B and Buckley JL** (2024) Sub-GHz wrist-worn antennas for wireless sensing applications: A review. *IEEE Open Journal of Antennas and Propagation* **5**, 1258–1281. https://doi.org/10.1109/OJAP.2024.3397193
13. **Ruaro A, Thaysen J and Jakobsen KB** (2016) Wearable shell antenna for 2.4 GHz hearing instruments. *IEEE Transactions on Antennas and Propagation* **64**(6), 2127–2135. https://doi.org/10.1109/TAP.2016.2543800.
14. **Orefice M, Pirinoli P and Dassano G** (2016) Electrically-small wearable antennas for emergency services applications. In *2016 International Workshop on Antenna Technologies (iWAT)*. Cocoa Beach, FL, USA. pp. 131–134. https://doi.org/10.1109/IWAT.2016.7434822.
15. **Virushabadoss N, Quaye R and Henderson R** (2019) Demonstration of electrically small antennas operating below 400 MHz. In *2019 IEEE International Symposium on Antennas and Propagation and USNC-URSI Radio Science Meeting*. Atlanta, GA, USA. pp. 1547–1548. https://doi.org/10.1109/APUSNCURSINRSM.2019.8889248.
16. **Hajj WE, Person C and Wiart J** (2013) A miniaturized rectangular-spiral bi-band coplanar antenna for off-body communications. In *2013 7th European Conference on Antennas and Propagation (EuCAP)*. Gothenburg. Sweden. pp. 3262–3265.
17. **Garcia E, Andújar A, Pijoan JL and Anguera J** (2024) Reconfigurable antenna booster system for multiband operation in IoT devices with an SP4T switch. *IEEE Open Journal of Antennas and Propagation*, 1–1. https://doi.org/10.1109/OJAP.2024.3359183
18. **Takanen N, Rasilainen K, Katajisto J, Pärssinen A and Soh PJ** (2025) Simulation and analysis of a reconfigurable electrically small antenna system for compact wearable devices. In *2025 18th European Conference on Antennas and Propagation (EuCAP)*. Stockholm, Sweden. pp. 1–5.
19. **Ban Y-L, Liu C-L, Chen Z, Li JL-W and Kang K** (2014) Small-size multiresonant octaband antenna for LTE/WWAN smartphone applications. *IEEE Antennas and Wireless Propagation Letters* **13**, 619–622.
20. **Paracha KN, Rahim SKA, Soh PJ and Khalily M** (2019) Wearable antennas: A review of materials, structures, and innovative features for autonomous communication and sensing. *IEEE Access* **7**, 56694–56712.
21. **Chu LJ** (1948) Physical limitations of omnidirectional antennas. *Journal of Applied Physics* **19**(12), 1163–1175.
22. **Wheeler HA** (1947) Fundamental limitations of small antennas. *Proceedings of the IRE* **35**(12), 1479–1484. https://doi.org/10.1109/JRPROC.1947.226199.
23. **Hansen RC** (1981) Fundamental limitations in antennas. *Proceedings of the IEEE* **69**(2), 170–182.
24. **McLean JS** (1996) A re-examination of the fundamental limits on the radiation *Q* of electrically small antennas. *IEEE Transactions on Antennas and Propagation* **44**(5), 672–676.
25. **Koutinos AG, Zekios CL, Georgakopoulos SV and Kyriacou GA** (2024) Increasing the bandwidth of antennas based on the frequency pulling technique: Theoretical limitations and practical considerations. *IEEE Transactions on Antennas and Propagation* **72**(5), 4064–4076. https://doi.org/10.1109/TAP.2024.3384771.
26. **Bittium** Bittium Faros™ - waterproof ECG devices for cardiac monitoring. https://www.bittium.com/medical/bittium-faros.
27. **Martens R, Safin E and Manteuffel D** (2011) Inductive and capacitive excitation of the characteristic modes of small terminals. In *2011 Loughborough Antennas & Propagation Conference (LAPC)*. Loughborough, UK. pp. 1–4.
28. **Cabedo-Fabres M, Antonino-Daviu E, Valero-Nogueira A and Bataller MF** (2007) The theory of characteristic modes revisited: A contribution to the design of antennas for modern applications. *IEEE Antennas and Propagation Magazine* **49**(5), 52–68.
29. **Vainikainen P, Ollikainen J, Kivekäs O and Kelander K** (2002) Resonator-based analysis of the combination of mobile handset antenna and chassis. *IEEE Transactions on Antennas and Propagation* **50**(10), 1433–1444. https://doi.org/10.1109/TAP.2002.802085.
30. **Ali SM and Payandehjoo K** (2014) Tunable antenna techniques for compact handset applications. *IET Microwaves, Antennas & Propagation* **8**(6), 401–408.
31. **Optenni Ltd**. Optenni Lab™: Circuit Synthesis Software for Antenna and RF Optimization. https://optenni.com.
32. **IEC/IEEE international standard** (2020) International standard - Measurement procedure for the assessment of specific absorption rate of human exposure to radio frequency fields from hand-held and body-mounted wireless communication devices – Part 1528: Human models, instrumentation, and procedures (frequency range of 4 MHz to 10 GHz). *IEC/IEEE 62209-1528: 2020* **1.0**, 1–284.
33. **Särestöniemi M, Singh D, Dessai R, Heredia C, Myllymäki S and Myllylä T** (2024) Realistic 3D phantoms for validation of microwave sensing in health monitoring applications. *Sensors* **24**, 1975.
34. **Sambandam P, Kanagasabai M, Mohammed GNA, Thirunavukkarasu M, Shanmuganathan S, Ramadoss S and Palaniswamy SK** (2020) Low profile pattern switchable multiband antenna for on/off body communication. *International Journal of RF and Microwave Computer-Aided Engineering* **30**(12), e22448. https://doi.org/10.1002/mmce.22448.
35. **Zradziński P, Karpowicz J and Gryz K** (2025) Assessing the antenna performance (radiated power) and electromagnetic impact (SAR) on a user of a wearable RF communication device, involving variously structured models. *IEEE Access* **13**, 19257–19265. https://doi.org/10.1109/ACCESS.2025.3528656.
36. **Atrash ME, Abdalla MA and Elhennawy HM** (2019) A wearable dual-band low profile high gain low SAR antenna AMC-backed for WBAN applications. *IEEE Transactions on Antennas and Propagation* **67**(10), 6378–6388.
37. **Ali U, Ullah S, Basir A, Kamal B, Matekovits L and Yoo H** (2023) Design and SAR analysis of AMC-based fabric antenna for body-centric communication. *IEEE Access* **11**, 73894–73911. https://doi.org/10.1109/ACCESS.2023.3295993.
38. **il Kwak S, Sim D-U, Kwon JH and Yoon YJ** (2017) Design of PIFA with metamaterials for body-SAR reduction in wearable applications. *IEEE Transactions on Electromagnetic Compatibility* **59**(1), 297–300. https://doi.org/10.1109/TEMC.2016.2593493.
39. **Soh PJ, Vandenbosch G, Wee FH, van den Bosch A, Martinez-Vazquez M and Schreurs D** (2015) Specific absorption rate (SAR) evaluation of textile antennas. *IEEE Antennas and Propagation Magazine* **57**(2), 229–240. https://doi.org/10.1109/MAP.2015.2414671

https://doi.org/10.1017/S1759078726103225 Published online by Cambridge University Press



Niklas Takanen received the M.Sc. degree in electrical engineering from the University of Oulu in 2024. His main research interests are antenna and circuit design.



Kimmo Rasilainen received the B.Sc. (Tech.), M.Sc. (Tech.) (Hons.), and D.Sc. (Tech.) degrees in electrical engineering from Aalto University, Espoo, Finland, in 2012, 2013, and 2017, respectively. From 2009 to 2017, he was with the Department of Electronics and Nanoengineering, School of Electrical Engineering, Aalto University, first as a Research Assistant and later as a Research Scientist, working on handset antennas and wireless sensors. From 2017 to 2020, he was a Postdoctoral Researcher with the Department of Microtechnology and Nanoscience, Chalmers University of Technology, Gothenburg, Sweden, working on the integration of mm-wave communications assemblies and thermal simulations. Since 2020, he has been a Postdoctoral Researcher with the Centre for Wireless Communications, University of Oulu, Finland, where he also teaches courses on radio engineering. He has authored or coauthored more than 50 international journal articles and conference papers. His current research interests include mm-wave and THz antennas, microwave engineering, material characterization, and thermal analysis.



Juha Katajisto received the M.Sc. degree in electrical engineering from the Tampere University of Technology, Tampere, Finland, in 2001. From 1998 to 2001, he was with the Telecommunications Laboratory, Tampere University of Technology, Finland, working on RFIC research. Since September 2001, he has been with Bittium (formerly Elektrobit), including its partners, Tampere, Finland, where he is currently a Principal Engineer of RF. At Bittium, he has been working on various R&D projects and wireless technologies within mobile phones, mobile satellite communications, wearable and IoT devices in consumer, medical, and industrial segments.



Aarno Pärssinen received the D.Sc. degree from the Helsinki University of Technology, Finland, in 2000. From 2000 to 2014, he was with the Nokia Research Center, Renesas Mobile, and Broadcom. Since 2014, he has been with the University of Oulu, Finland, where he is currently a Professor. His research interests include transceiver architectures and RFICs. He has authored or coauthored more than 250 international publications and holds several patents. From 2007 to 2017, he was a member of the technical program committee of ISSCC. Since 2024, he has been a member of the technical program committees of the RFIC Symposium and ESSERC. He is one of the original contributors of the Bluetooth low energy extension, now called BT LE, and one of the research area leads of the national 6G flagship program in Finland. Dr. Pärssinen is an IEEE Fellow for contributions to direct conversion, digital RF transceivers, and hardware-aware communications systems.



Ping Jack Soh received the Ph.D. degree in electrical engineering from KU Leuven, Leuven, Belgium, in 2013. He is currently a Professor with the University of Oulu, Oulu, Finland, and an Academy Research Fellow with the Research Council of Finland. He started his career in the electronics/telecommunication industry as a Test Engineer (2002–2004) and an R&D Engineer (2005–2006). He was then a Research Assistant (2009–2013), Postdoctoral Research Fellow (2013–2014), and a Research Affiliate (since 2014) at KU Leuven's ESAT-WaveCoRE research group. In Oulu, he was also the coordinator for the "Devices and Circuit Technology" strategic research area within Finland's 6G Flagship national research program (2022–2023). His research interests include antennas, arrays, and metasurface design, and their applications in wearable/implantable devices; next-generation communications; compact satellites; EM safety and absorption; and wireless techniques for healthcare.

https://doi.org/10.1017/S1759078726103225 Published online by Cambridge University Press